Autonomous Ground Vehicle Navigation Using Integrated GPS and Laser-scanner Measurements

Mathieu Joerger and Boris Pervan
Illinois Institute of Technology
10 W 32nd Street
Chicago, IL, 60616 USA

Abstract- **This paper describes the design, analysis and testing of a navigation system based on combined GPS and laser-scanner measurements. Using carrier phase differential GPS, centimeter-level positioning of autonomous ground vehicles (AGVs) is achievable. However, GPS signals are easily attenuated or blocked, so their use is generally restricted to open-sky areas. In response, in this work we augment GPS with two-dimensional laser-scanner measurements. The latter are available when GPS is not, and provide in addition, a means for obstacle detection.**

Laser measurements are processed using a Simultaneous Localization And Mapping (SLAM) procedure. Vehicle and landmark position estimation is performed simultaneously using an extended Kalman filter; we address the data association problem, which establishes correspondences between consecutive sets of measurements and a continuously updated map of landmarks. The resulting laser-based SLAM solution is carefully analyzed by identifying and isolating the individual effects of the joint angular and ranging measurements, the combination of measurements from multiple landmarks, the correlation between vehicle and landmark position estimates, and the uncertainty on the vehicle's heading angle.

A detailed covariance analysis is then carried out in order to quantify the sensitivity of the vehicle's position estimate error to the vehicle's velocity, the landmark geometry, and the laser's range limit. Further sensitivity analyses are structured around two scenarios: first, a 'forest scenario' where the vehicle roves across a GPS-unavailable area using tree trunks as landmarks in order to maintain a precise position estimate; second, an 'urban canyon' scenario describing how we can make use of GPS signals that alone are too few to generate a position fix, by utilizing additional laser measurements to buildings' edges. Finally, experimental results using a prototype AGV are presented to validate the navigation system performance.

I. INTRODUCTION

This paper describes the design, analysis and testing of a navigation system based on combined Global Positioning System (GPS) and laser-scanner measurements. In order to fully exploit the complementary properties of the two sensors, their measurements are integrated in the range domain. The performance of the resulting positioning and mapping algorithm exceeds that of position-domain integration, especially in places such as urban canyons, where fewer than four GPS satellite signals are available.

The algorithm presented in this work is intended to be used on an outdoor autonomous ground vehicle (AGV). AGVs can support missions that are unsafe or too difficult for human operation. In 1997, O'Connor [1] and Bell [2], set the path for the development and expansion of GPS-based automated vehicle control techniques in practical applications. They successfully realized the automated control of a tractor for unmanned agricultural field plowing. Since then, in less than a decade, precision-controlled AGVs have been successfully implemented in outdoor applications such as ramming of ski runs [3], surveillance missions [4] or intelligent traffic management [5]. More recently, the multiple successes at the "DARPA Grand Challenge" have placed AGV navigation in the forefront and further widened the scope of their potential applications.

Carrier-Phase Differential GPS (CPDGPS) provides centimeter-level accuracy, which is critical for many of these precision applications. However, robust CPDGPS navigation requires good sky visibility because GPS satellite ranging signals can be significantly attenuated or blocked by buildings, trees, and rugged terrain. In response, we augment GPS with two-dimensional laser-scanner measurements from surrounding obstacles, which are used as landmarks. Laser information is available when GPS is not, and provides in addition, a means for obstacle detection.

Dead reckoning sensors, in particular inertial navigation instruments, are often used to bridge gaps in GPS satellite availability, but these sensors drift over time [6]. In contrast, the laser-based positioning error increases with distance – as earlier landmarks get out of the scanner's range and new landmarks come in sight. Ranging source devices such as lasers can maintain sub-meter accuracy over several hundreds of meters, which, at land-vehicle speeds, is rarely the case even for high quality inertial systems. Occasional GPS updates are used here to correct this laser-based positioning drift.

Therefore, one of the primary objectives of this research is to evaluate the length of GPS-outages that the proposed navigation system can manage while maintaining sub-meter accuracy. The second objective is to compare the system's performance with respect to more traditional position-domain algorithms. Indeed, more than enabling precise positioning over extended areas, the range-domain integration makes use of GPS signals that alone are too few to generate a position fix.

In this work, laser measurements are processed using an Extended Kalman Filter (EKF) based Simultaneous Localization And Mapping (SLAM) procedure. In addition, range-domain integration of GPS and laser measurements necessitates that we derive a unified cycle ambiguity and position estimation process. This is realized in a compact formulation using a measurement-differencing filter. A sensitivity analysis based on covariance and Monte-Carlo simulations is then carried out to identify the most influential parameters and quantify their impact on the navigation performance. Finally, experimental testing in a structured environment demonstrates the efficiency of the system.

II. Laser-based SLAM

A. Concept and Algorithm

The terms SLAM and Concurrent Mapping and Localization (CML) [7] refer to the problem of vehicle positioning using previously unknown features in the environment. Over the past two decades, several alternative solutions to the SLAM problem [8] have emerged. We selected an EKF approach, which provides an incremental solution and can therefore be utilized in real time.

In this case, the complete solution to the laser-based SLAM problem includes the following tasks:

- raw measurement processing, in which we include noise rejection, segmentation and feature extraction; these algorithms consist in extracting or selecting one measurement per landmark, out of the hundreds which constitute a laser scan
- data association, which aims at determining from which landmark the extracted measurement is originating from, and
- vehicle and landmark position estimation, which is here performed simultaneously using an EKF.

The first two tasks are achievable even in outdoor environments with high obstacle densities, but they require complex algorithms [9]. In order to keep the focus of this paper on the range-domain integration of GPS and laser measurements we select simple but efficient procedures and consider environments with static landmarks at locations sparse enough to be distinguishable. Also in the forthcoming covariance analyses of Sections II.B and IV, we assume that both measurement processing and data association are successfully realized.

Notice that map-management [10] procedures are not an issue here since, as opposed to robotic mapping applications, landmark positioning is an induced problem (the primary objective here is vehicle positioning) so that map-feature storage is minimal.

The EKF approach to the SLAM problem is based on the simultaneous estimation of vehicle states (composed of the two dimensional position coordinates x_V and y_V in a local reference frame, and of the heading ϕ_V) and landmark states (position coordinates p_X^i and p_Y^i for $i = 1...n_L$ with n_L being the number of landmarks under consideration). The two-dimensional vehicle and landmark model is shown in Fig. 1.

In order to study the navigation performance based solely on sensor information (without a vehicle dynamic model), we inflate the covariance of the vehicle-position process noise $\mathbf{w_V}$ (gaussian purely random vector). The landmarks are stationary, hence the discrete-time process equation is:

$$\begin{bmatrix} \mathbf{x_V} \\ \mathbf{p} \end{bmatrix}_{k+1} = \begin{bmatrix} \mathbf{I^3} & \mathbf{0} \\ \mathbf{0} & \mathbf{I^{n_L}} \end{bmatrix} \begin{bmatrix} \mathbf{x_V} \\ \mathbf{p} \end{bmatrix}_k + \begin{bmatrix} \mathbf{w_V} \\ \mathbf{0} \end{bmatrix}_k \tag{1}$$

where $\mathbf{x_V} = \begin{bmatrix} x_V & y_V & \phi_V \end{bmatrix}^\mathbf{T}$,

$$\mathbf{p} = \begin{bmatrix} p_X^1 & p_Y^1 & \mathbf{i} & p_X^{n_L} & p_Y^{n_L} \end{bmatrix}^\mathbf{T}$$

and $\mathbf{I^n}$ is a $n \times n$ identity matrix

The vehicle is equipped with a 360° laser-scanner (in practice we use two 180° laser-scanners mounted back-to-back). As a result of the point-feature extraction routine, we obtain one angular and one ranging measurement per landmark, respectively:

$$\theta^i = -\arctan\left(\frac{p_X^i - x_V}{p_Y^i - y_V}\right) - \phi_V + \nu_\theta \tag{2}$$

$$d^i = \sqrt{\left(p_X^i - x_V\right)^2 + \left(p_Y^i - y_V\right)^2} + \nu_d \tag{3}$$

ν_θ and ν_d are gaussian distributed white measurement noise values. Their standard deviations are determined based on the manufacturer specifications in Table I and on experimental data.

Equations (2) and (3) are linearized using the first order terms of their Taylor expansions, so that the matrix form of angular and ranging measurement deviations is:

$$\begin{bmatrix} \boldsymbol{\delta d} \\ \boldsymbol{\delta\theta} \end{bmatrix} = \begin{bmatrix} \mathbf{F_d(j)} & \mathbf{0} & \mathbf{F_d(I)} \\ \mathbf{F_\theta(j)} & \mathbf{-1^{n_L}} & \mathbf{F_\theta(I)} \end{bmatrix} \begin{bmatrix} \boldsymbol{\delta x_{V,POS}} \\ \delta\phi_V \\ \boldsymbol{\delta p} \end{bmatrix} + \begin{bmatrix} \boldsymbol{\nu_d} \\ \boldsymbol{\nu_\theta} \end{bmatrix} \tag{4}$$

where $\mathbf{1^n}$ is a $n \times 1$ column vector filled with 1's.

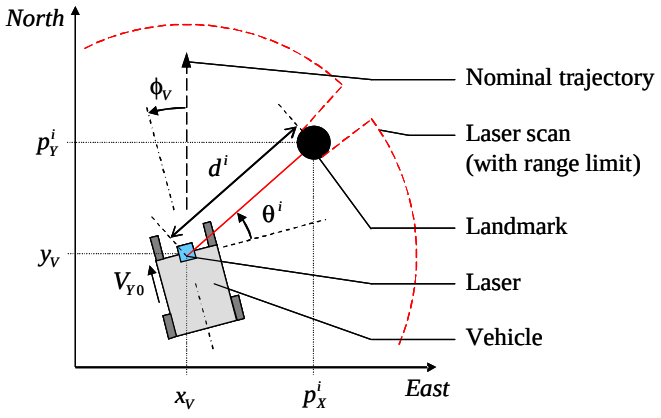

Fig. 1. Vehicle and landmark model.

TABLE I
LASER-SCANNER (SICK LMS200) SPECIFICATIONS

Parameters	Values
Range Limit	8m to 30m (mm-mode) 80m (cm-mode)
Scanning angle	180°
Ranging accuracy (standard deviation)	0.01m (mm-mode) 0.05m (cm-mode)
Angular resolution	0.5°
Update rate	5 Hz

The matrices $\mathbf{F_d}(\mathbf{j})$, $\mathbf{F_\theta}(\mathbf{j})$, $\mathbf{F_d}(\mathbf{l})$ and $\mathbf{F_\theta}(\mathbf{l})$ are expressed in Appendix I.

B. Covariance Analysis of the SLAM Solution

In an effort to understand the SLAM process, we carry out an example covariance analysis in four steps. As illustrated in Fig. 2, we isolate the individual effects of (a) the joint angular and ranging measurements, (b) the combination of measurements from multiple landmarks, (c) the correlation between vehicle and landmark position estimates, and (d) the uncertainty on the vehicle's heading angle. For all cases, the vehicle starts with an initial position estimate (subsequently provided by GPS) and passes by landmarks while roving along the Y-axis.

To begin the analysis, we assume that the landmark position and the vehicle heading are known. Fig. 2.a) presents the case of a single obstacle. The result translates the values given to the angular and ranging measurement noise covariances.

Fig. 2.b) illustrates the combination of measurements from two landmarks symmetrically located with respect to the trajectory. The combined solution coincides with the intersection of the dashed ellipses because measurements from different landmarks are independent.

In Fig. 2.c), we no longer assume that the locations of the landmarks are known. The positioning error on the landmarks decreases steadily because landmarks are stationary. Both measurement averaging and geometry change due to the vehicle motion contribute to the estimation process. Landmarks that are closer to the trajectory contribute more to the in-track coordinate estimation than to the cross-track coordinate. Because the laser is limited in range, the uncertainty on the cross-track state is always drifting more rapidly. This is why in the remainder of the paper, we use the vehicle cross-track position estimate as navigation performance criterion.

Finally in Fig.2.d), we no longer assume that the vehicle heading is known. The performance is dramatically poorer. Unlike in the previous case, there is not enough information here to significantly improve the landmark state estimates. This is one situation in which, in the next sections, we will be able to exploit the integration of GPS measurements to evaluate the initial landmarks' positions, hence considerably improving this result.

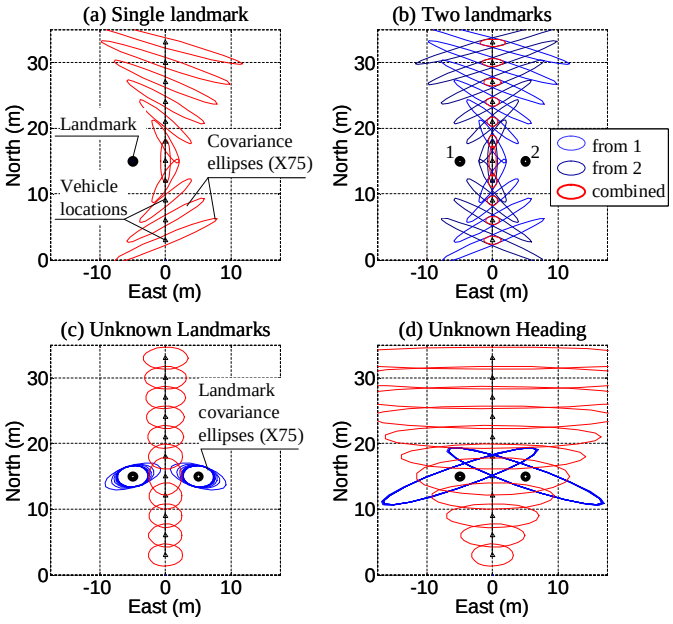

Fig. 2. Four-step covariance analysis.

Additional heading information can be provided using a dynamic model for the vehicle, or using sensors such as encoders or magnetometers. The resulting corrected drift in cross-track position, using an example magnetic compass with a 1° standard deviation (commercially available), is presented, is presented in Fig. 3.

III. GPS ALGORITHM AND RANGE-DOMAIN INTEGRATION

In this section, we derive a compact formulation for a combined GPS cycle ambiguity and position estimation process and present the mathematics behind the laser/GPS range-domain integration. The details of the derivation are not necessary to understand the more intuitive description of the system provided in Sections IV to VI, which is based on a performance analysis.

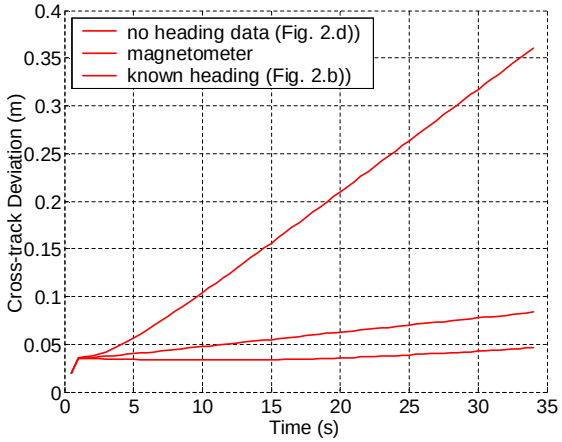

Fig. 3. Influence of the heading-angle uncertainty.

A. Prior work: separate integer and position estimation

In previous research, we designed a navigation and control system for an AGV [11], which we used for lawn-mowing applications [12]. Real-time cm-level positioning is achieved using differential code and carrier-phase (CP) measurements, which can be expressed as:

$$PR^i = -\mathbf{e}_\mathbf{i}^\mathbf{T}\mathbf{x}_\mathbf{V} + \tau + \xi^i{}_{PR} \tag{5}$$

$$CP^i = -\mathbf{e}_\mathbf{i}^\mathbf{T}\mathbf{x}_\mathbf{V} + \tau + N^i + \xi^i{}_{CP} \tag{6}$$

where $\mathbf{e_i}$ is the unit line-of-sight vector to satellite i, N^i is the differential CP integer cycle ambiguity, and τ is the differential GPS clock bias. Here, we note:

$$\mathbf{x_V} = \begin{bmatrix} x_V & y_V & z_V \end{bmatrix}^\mathbf{T}$$

$\xi^i{}_{PR}$ and $\xi^i{}_{CP}$ are the differential code and CP time-correlated measurement noises (with standard deviations $\sigma_{\xi,PR}$ and $\sigma_{\xi,CP}$ respectively). Their correlation, which is due to multipath reflections, is given a time constant T_M.

Our former navigation system was composed of two separate processes [13].

- The integer estimation procedure is a Kalman Filter (KF) measurement update performed at regular intervals equal to $2T_M$. Measurements taken at these intervals are assumed to be uncorrelated.
- A weighted least squares (WLS) solution provides position estimation at each sample time T_S using the incoming measurements and the latest cycle ambiguity estimate.

In the perspective of range-domain integration with laser data, this dual-stage procedure is not an optimal solution. Indeed, the WLS process does not handle prior information, and the multipath correlation prevents measurement updates from being performed more frequently.

B. Single-stage integer and position estimation

In order to implement frequent GPS filtering updates, we model the colored measurement noise as a first order Gauss Markov process:

$$\begin{aligned} \xi^i{}_{PR}(t_{k+1}) &= e^{(-T_S/T_M)} \cdot \xi^i{}_{PR}(t_k) + \nu^i{}_{PR}(t_k) \\ \xi^i{}_{CP}(t_{k+1}) &= e^{(-T_S/T_M)} \cdot \xi^i{}_{CP}(t_k) + \nu^i{}_{CP}(t_k) \end{aligned} \tag{7}$$

where $t_{k+1} = t_k + T_S$, and $\nu^i{}_{PR}(t_k)$ and $\nu^i{}_{CP}(t_k)$ are purely random sequences with variances $\sigma^2_{\nu,PR/CP} = \left(1 - e^{-2(T_S/T_M)}\right)\sigma^2_{\xi,PR/CP}$. In general, we use the notation v^i to designate the i^{th} element of a vector $\mathbf{v}$. Hence, from (7):

$$\boldsymbol{\xi}_{\mathbf{k+1}} = \boldsymbol{\Psi}\boldsymbol{\xi}_\mathbf{k} + \mathbf{v}_\mathbf{k}$$

where $\boldsymbol{\Psi}$ is called the correlation matrix, and the measurement $\mathbf{z}$ is expressed as:

$$\mathbf{z}_\mathbf{k} = \mathbf{H}_\mathbf{k}\mathbf{x}_\mathbf{k} + \boldsymbol{\xi}_\mathbf{k}$$

where $\mathbf{x}$ is the state vector and $\mathbf{H}$ is the observation matrix.

In this work, we use a measurement-differencing filter, which is first introduced in 1968 by Bryson and Henrikson as a way to model correlated measurement noise in a state space representation [14]. It is an efficient alternative to state augmentation because the number of states remains unchanged and the measurement noise matrix is no longer singular. The core idea defining this filter is the use of a pseudo-measurement $\mathbf{z}^\mathbf{r}_\mathbf{k}$:

$$\begin{aligned} \mathbf{z}^\mathbf{r}_\mathbf{k} &= \mathbf{z}_{\mathbf{k+1}} - \boldsymbol{\Psi}\mathbf{z}_\mathbf{k} \\ &= \left(\mathbf{H}_{\mathbf{k+1}}\boldsymbol{\Phi} - \boldsymbol{\Psi}\mathbf{H}_\mathbf{k}\right)\mathbf{x}_\mathbf{k} + \mathbf{H}_{\mathbf{k+1}}\mathbf{w}_\mathbf{k} + \mathbf{v}_\mathbf{k} \\ &= \mathbf{H}^\mathbf{r}_\mathbf{k}\mathbf{x}_\mathbf{k} + \mathbf{v}^\mathbf{r}_\mathbf{k} \end{aligned} \tag{8}$$

where $\mathbf{w}$ is the process noise vector, and $\boldsymbol{\Phi}$ is the system matrix. We have:

$$\mathbf{v}^\mathbf{r}_\mathbf{k} = \mathbf{H}_{\mathbf{k+1}}\mathbf{w}_\mathbf{k} + \mathbf{v}_\mathbf{k} \quad \text{and} \quad \mathbf{H}^\mathbf{r}_\mathbf{k} = \mathbf{H}_{\mathbf{k+1}}\boldsymbol{\Phi} - \boldsymbol{\Psi}\mathbf{H}_\mathbf{k} \tag{9}$$

The correlated measurement noise vector $\boldsymbol{\xi}_\mathbf{k}$ cancels out in the pseudo-observation equation (8), thus $\mathbf{v}^\mathbf{r}_\mathbf{k}$ is a white sequence.

Next, in order to eliminate the correlation that now exists between the pseudo-measurement noise $\mathbf{v}^\mathbf{r}_\mathbf{k}$ and the process noise $\mathbf{w}_\mathbf{k}$, we use the pseudo-process equation:

$$\begin{aligned} \mathbf{x}_{\mathbf{k+1}} &= \left(\boldsymbol{\Phi} - \mathbf{D}_\mathbf{k}\mathbf{H}^\mathbf{r}_\mathbf{k}\right)\mathbf{x}_\mathbf{k} + \mathbf{D}_\mathbf{k}\mathbf{z}^\mathbf{r}_\mathbf{k} + \mathbf{w}_\mathbf{k} - \mathbf{D}_\mathbf{k}\mathbf{v}^\mathbf{r}_\mathbf{k} \\ &= \boldsymbol{\Phi}^\mathbf{r}\mathbf{x}_\mathbf{k} + \mathbf{D}_\mathbf{k}\mathbf{z}^\mathbf{r}_\mathbf{k} + \mathbf{w}^\mathbf{r}_\mathbf{k} \end{aligned} \tag{10}$$

where $\mathbf{z}^\mathbf{r}_\mathbf{k}$ is considered a deterministic input. We used the expressions for the pseudo-process matrix and noise vector:

$$\boldsymbol{\Phi}^\mathbf{r} = \boldsymbol{\Phi} - \mathbf{D}_\mathbf{k}\mathbf{H}^\mathbf{r}_\mathbf{k} \quad \text{and} \quad \mathbf{w}^\mathbf{r}_\mathbf{k} = \mathbf{w}_\mathbf{k} - \mathbf{D}_\mathbf{k}\mathbf{v}^\mathbf{r}_\mathbf{k}. \tag{11}$$

In order for $\mathbf{v}^\mathbf{r}_\mathbf{k}$ and $\mathbf{w}^\mathbf{r}_\mathbf{k}$ to be uncorrelated, we take:

$$\mathbf{D}_\mathbf{k} = \mathbf{W}\mathbf{H}^\mathbf{T}_\mathbf{k}\left(\mathbf{V}^\mathbf{r}\right)^{-1}$$

where $\mathbf{W}$ and $\mathbf{V}^\mathbf{r}$ are the covariance matrices corresponding respectively to $\mathbf{w}$ and $\mathbf{v}^\mathbf{r}$. Bryson provides a detailed and elegant derivation of this result in [15].

Equations (8) and (10) constitute a state-space representation, whose state vector can be estimated using a KF (e.g. [16]). Nevertheless, one crucial difference with traditional implementations is the interpretation of the filter's solution with respect either to the pseudo-measurement $\mathbf{z}^\mathbf{r}$, or to the actual measurement $\mathbf{z}$, in which we are interested here.

If we use the notation $\hat{\mathbf{x}}^\mathbf{r}_{\mathbf{k/k}}$ to designate the best estimate of $\mathbf{x}$ at time t_k knowing $\mathbf{z}^\mathbf{r}_\mathbf{k}$, and $\hat{\mathbf{x}}_{\mathbf{k/k}}$ for the best estimate of $\mathbf{x}_\mathbf{k}$ knowing $\mathbf{z}_\mathbf{k}$, then according to (8), we can write the equivalences:

$$\hat{\mathbf{x}}^\mathbf{r}_{\mathbf{k/k}} \equiv \hat{\mathbf{x}}_{\mathbf{k/k+1}} \text{ and } \hat{\mathbf{x}}^\mathbf{r}_{\mathbf{k+1/k}} \equiv \hat{\mathbf{x}}_{\mathbf{k+1/k+1}}$$

Refer to [14] for more details. For ease of notation, we use $\hat{\mathbf{x}}_\mathbf{k} = \hat{\mathbf{x}}_{\mathbf{k/k}}$ and $\underline{\mathbf{x}}_\mathbf{k} = \hat{\mathbf{x}}_{\mathbf{k\text{-}1/k}}$. As a result, the KF estimation equations are:

$$\underline{\mathbf{x}}_\mathbf{k} = \hat{\mathbf{x}}_{\mathbf{k\text{-}1}} + \mathbf{K}_\mathbf{k}\left(\mathbf{z}^\mathbf{r}_\mathbf{k} - \mathbf{H}^\mathbf{r}_\mathbf{k}\hat{\mathbf{x}}_{\mathbf{k\text{-}1}}\right) \tag{12}$$

$$\hat{\mathbf{x}}_\mathbf{k} = \boldsymbol{\Phi}^\mathbf{r}\underline{\mathbf{x}}_\mathbf{k} + \mathbf{D}_\mathbf{k}\mathbf{z}^\mathbf{r}_\mathbf{k} \tag{13}$$

And the actual prediction $\bar{\mathbf{x}}_{k+1}$ is obtained from

$$\bar{\mathbf{x}}_{k+1} = \mathbf{\Phi}\hat{\mathbf{x}}_k \,, \quad \text{with covariance} \quad \bar{\mathbf{P}}_{k+1} = \mathbf{\Phi}\hat{\mathbf{P}}_k\mathbf{\Phi}^T + \mathbf{W} \,.$$

As a conclusion, the state efficiency of the measurement differencing filter is well worth the cost of a few complications in the implementation (storage of $\mathbf{z}_{k-1}$ and $\mathbf{H}_{k-1}$ and initialization procedure). Indeed, when processing code and CP measurements from a 12-channel dual-frequency receiver, a state augmented filter requires 48 additional states.

C. *Integration of GPS and laser-scanner measurements*

For consistency with the interpretation of $\hat{\mathbf{x}}$ and $\bar{\mathbf{x}}$, we apply the same measurement differencing equation (8) to the laser-scanner data (for which $\mathbf{\Psi} = \mathbf{0}$). Note briefly that, with regard to management routines, landmark states are treated differently than cycle-ambiguity states [17] because their value after reacquisition does not change. The complete laser-augmented GPS navigation system in matrix form is:

$$\begin{bmatrix} \mathbf{x}_V \\ \mathbf{N} \\ \mathbf{p} \end{bmatrix}_{k+1} = \begin{bmatrix} \mathbf{\Phi}_V & & \mathbf{0} \\ & \mathbf{I}^{n_S} & \\ \mathbf{0} & & \mathbf{I}^{n_L} \end{bmatrix} \begin{bmatrix} \mathbf{x}_V \\ \mathbf{N} \\ \mathbf{p} \end{bmatrix}_k + \begin{bmatrix} \mathbf{w} \\ \mathbf{0} \\ \mathbf{0} \end{bmatrix}_k \tag{14}$$

$$\begin{bmatrix} \mathbf{PR} \\ \mathbf{CP} \\ \mathbf{d} \\ \boldsymbol{\theta} \end{bmatrix}_k = \begin{bmatrix} \mathbf{G} & \mathbf{0} & \mathbf{1}^{n_S} & \mathbf{0} & \mathbf{0} \\ \mathbf{G} & \mathbf{0} & \mathbf{1}^{n_S} & \mathbf{I}^{n_S} & \mathbf{0} \\ \mathbf{F}_d(\mathbf{j}) & \mathbf{0} & \mathbf{0} & \mathbf{0} & \mathbf{F}_d(\mathbf{I}) \\ \mathbf{F}_\theta(\mathbf{j}) & -\mathbf{1}^{n_L} & \mathbf{0} & \mathbf{0} & \mathbf{F}_\theta(\mathbf{I}) \end{bmatrix} \begin{bmatrix} \mathbf{x}_{V,POS} \\ \phi_V \\ \tau \\ \mathbf{N} \\ \mathbf{p} \end{bmatrix}_k + \begin{bmatrix} \boldsymbol{\xi}_{PR} \\ \boldsymbol{\xi}_{CP} \\ \mathbf{v}_d \\ \mathbf{v}_\theta \end{bmatrix}_k \tag{15}$$

where $\mathbf{G} = \begin{bmatrix} -\mathbf{e}_1 & \mathbf{i} & -\mathbf{e}_{n_S} \end{bmatrix}^T$,

and $\mathbf{\Phi}_V$ is the vehicle system matrix. In this case, we note:

$$\mathbf{x}_V = \begin{bmatrix} \mathbf{x}_{V,POS}^T & \phi & \tau \end{bmatrix}^T, \quad \text{with} \quad \mathbf{x}_{V,POS} = \begin{bmatrix} x_V & y_V & z_V \end{bmatrix}^T$$

where the altitude z_V is constant in this work.

Equations (14) and (15) constitute a state-space representation written in the form:

$$\mathbf{x}_{k+1} = \mathbf{\Phi}\mathbf{x}_k + \mathbf{w}_k \quad \text{and} \quad \mathbf{z}_k = \mathbf{H}_k\mathbf{x}_k + \mathbf{v}_k \,,$$

where some elements of $\mathbf{v}_k$ are correlated. We use the measurement differencing filter described in (8), (9) and (11) to (13) to estimate the state vector $\mathbf{x}_k$.

IV. Covariance Analysis

A. *The 'forest scenario'*

The use of AGVs for landmine detection and removal is particularly well suited because of the dangerous, tedious and repetitive nature of the task [18]. Minefields include wooded environments in which GPS is unavailable, hence this 'forest scenario': the AGV starts in a GPS-available area (yellow in Fig. 4.a)) and roves across a GPS-unavailable zone (blue)

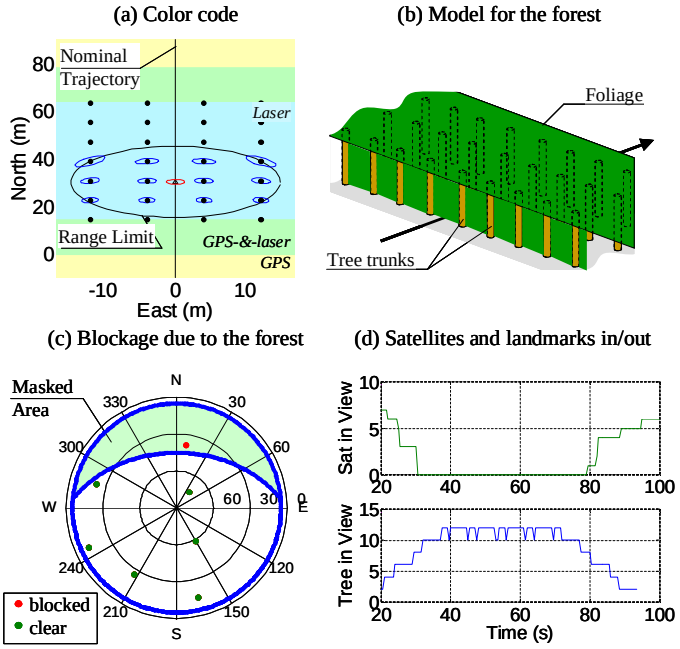

Fig. 4. Model for the forest and resulting masking.

using tree-trunks as landmarks. This sub-section aims at identifying the most sensitive parameters and quantifying the navigation performance as a function of the GPS-outage distance. We address the decisive role of the transitional GPS-and-laser-available area (green).

The model for the forest is illustrated Fig. 4.b) and a snap-shot of the azimuth-elevation mask for a GPS receiver on the ground is shown in Fig. 4.d). The resulting position covariance over time is plotted in Fig. 5). Remember that in this section, we assume that feature extraction and data association are successfully achieved. Smooth transitions are successfully realized from one colored area to another. As expected from the analysis in Section II.B, the cross-track error drifts more rapidly than for the in-track coordinate.

To further investigate the individual effects of the model's parameters, we conduct a sensitivity analysis with respect to a nominal configuration (given at the bottom of Table II).

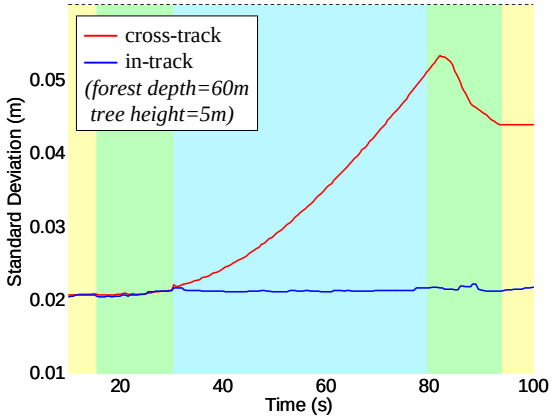

Fig. 5. Covariance result over time.

TABLE II
SENSITIVITY ANALYSIS

Configuration	Covariance Result (m)	Monte-Carlo Results (m)
Nominal*	0.095	0.175
Tree height = 5m	0.0924	0.147
Tree density = 0.003 tree/m^2	0.123	0.198
AGV velocity: V_{Y0} = 3m/s	0.139	0.394
Laser range Limit = 20m	0.057	0.148
Using a magnetometer	0.076	0.083
*: tree height = 10m, tree density = 0.015, V_{Y0} = 1m/s, range limit = 15m forest depth = 100m, no magnetometer		

Again, the performance criterion is the cross-track deviation at the exit of the laser-only (blue) area where the value is usually close to its maximum. Most of the results (listed in the 2nd column) have logical explanations: for example, a larger laser range-limit generates more measurements hence better positioning accuracy. A higher vehicle velocity and a lower tree density have the opposite effect. And as mentioned earlier, a significant improvement is gained from the use of additional information from a heading sensor.

The plot in Fig. 6 suggests that, for the nominal configuration, better than 0.5m cross-track accuracy is maintained over GPS-outages larger than 300 meters (assuming systematically successful data association unlike for the Monte-Carlo results – more in Section V). For the nominal configuration and for the many listed in Table II, the laser/GPS navigation system extends the availability of sub-meter navigation solutions over hundreds of meters, as compared to non-augmented implementations.

Finally, the uncertainty on the position of trees when entering the blue area determines the vehicle positioning accuracy throughout the GPS outage (Section II.B). Now, the tree height defines the GPS mask, and hence the frontier between the blue and green areas. Therefore we obtain better results in forests with lower trees (Table II). To further study the navigation performance in this transitional area, we consider an 'urban canyon scenario'.

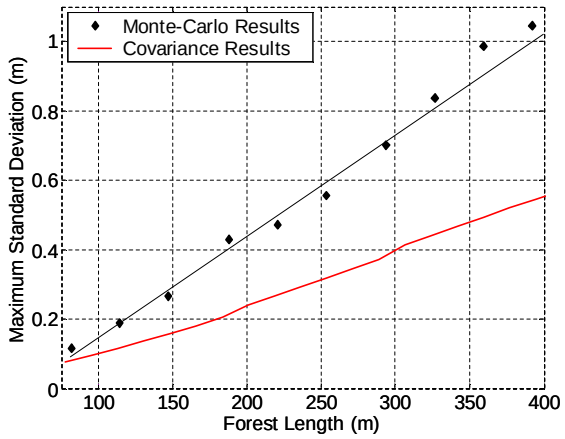

Fig. 6. Performance vs. length of the GPS-outage.

B. *The 'urban canyon scenario'*

GPS solutions are rarely available in urban canyons or forest roads because of the severe sky-blockage caused by bordering buildings and trees. The distinctive advantage of the range-domain integration is best illustrated here since the estimation process makes use of GPS signals that alone would be too few to generate a position fix. This sub-section aims at quantifying the navigation improvement brought by these few additional GPS signals as compared to a position-domain integration.

We make the assumption that signals with a clear line of sight are not corrupted despite potential multipath interferences in real-life scenarios. Fig. 7 describes the model used to recreate urban canyon conditions. Laser measurements are extracted at the buildings' edges.

First, in order to evaluate the number of GPS signals available as a function of the model's parameters, we perform a satellite availability analysis. We determine the number of satellites with a clear line of sight to the AGV over 24 hours at one minute intervals. The selected location is Chicago. We repeat the operation for different street orientations (in increments of 45°), and for five different locations with respect to the center of the street (to recreate different traffic lanes). The resulting composite satellite availability plot (Fig. 8) reveals striking results: for building heights of 50 meters, GPS position fixes are available in only 2% of the cases. In 15% and 40% of the cases, there are respectively 3 and 2 satellites available, which are left unused with non-augmented GPS navigation algorithms. Note that one satellite is useless because of the undetermined GPS clock bias, whereas two are enough to augment the laser data because we assume a constant altitude.

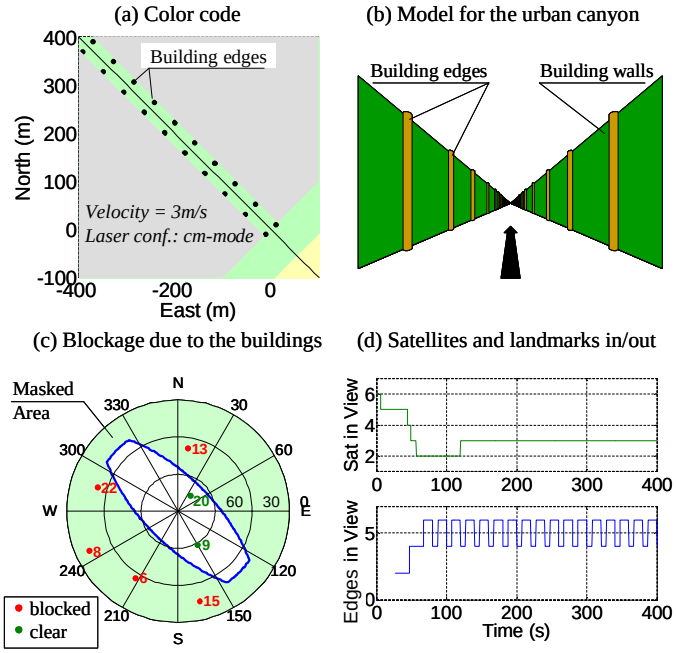

Fig. 7. Model for the urban canyon and resulting masking.

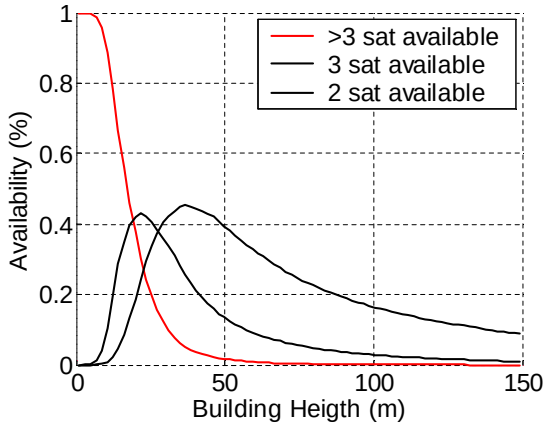

Fig. 8. Composite satellite availability.

The estimated cross-track standard deviation for three types of implementations is given Fig. 9. As explained in Section II.B, the laser-based solution drifts very rapidly, even with the added magnetometer data. In the case of the range-domain integration however, the two or three GPS signals available are enough to maintain and even correct the drift, hence enabling to sustain precise absolute positioning. This very dramatic change in the results illustrates the terrific advantage of the range-domain integration over position-domain algorithms.

V. Direct Simulations

Practical implementations of SLAM necessitate that we address the raw laser measurement processing, which includes raw data filtering, segmentation and feature extraction, and the data association. These algorithms aim at selecting the measurements that are fed into the EKF, and identifying the states to which they provide observations. They are succinctly described here but more details are available in Appendix II.

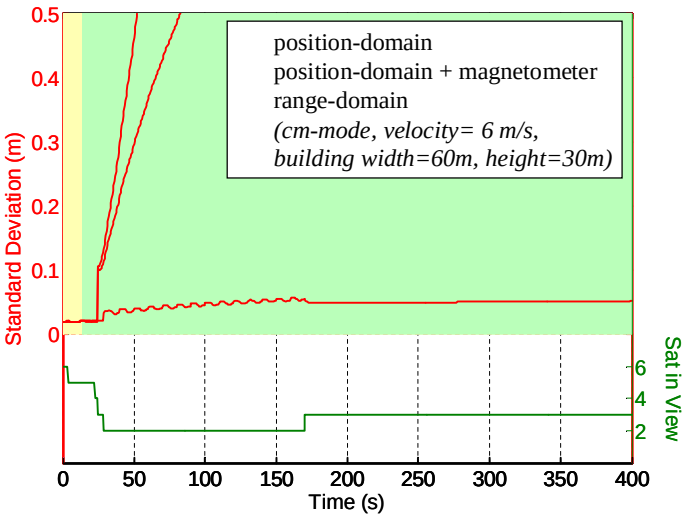

Fig. 9. Comparison of position-domain and range-domain integrations

A laser scan is composed of hundreds of ranging measurements at regular angular intervals. First, a noise-rejection algorithm eliminates the non-gaussian noise present in the raw data (see Fig. 10). Then, segments of the laser-scan corresponding to landmarks are identified and point-features (here the center of a cylinder in the plane of the scan) are extracted. Finally, the extracted measurements are associated with their corresponding landmarks. Failures to extract a measurement or to associate it increase the vehicle positioning error (which explains differences between the covariance and Monte-Carlo results).

In this section, we implement these procedures for the forest scenario, and use the resulting navigation performance to refine the conclusions of the covariance analysis.

In order to simulate the effects of process disturbances, we use a straightforward vehicle kinematic model:

$$x_V = -V_{Y0}\sin(\phi_V), \quad y_V = V_{Y0}\cos(\phi_V)$$

which is linearized for small values of ϕ_V. The process noise values are selected to reproduce the experimental conditions, in which the AGV is remotely controlled.

Similarly, the measurements are designed to be representative of real observations as illustrated Fig. 11.a). The non-linear measurement equations (2) and (3) are used in the estimation process, which now includes an input vector $\mathbf{u}$. Because of the non-linearities, we chose to rewrite the KF equations (12) and (13) in the form:

$$\underline{\mathbf{x}}_k = \hat{\mathbf{x}}_{k-1} + \mathbf{K}_k\left(\mathbf{z}_k^r - \mathbf{h}^r\left(\hat{\mathbf{x}}_{k-1}, \overline{\mathbf{x}}_k\right)\right)$$

$$\hat{\mathbf{x}}_k = \mathbf{\Phi}\underline{\mathbf{x}}_k + \mathbf{D}_k\left(\mathbf{z}_k^r - \mathbf{h}^r\left(\underline{\mathbf{x}}_k, \mathbf{\Phi}\underline{\mathbf{x}}_k + \mathbf{u}_k\right)\right) + \mathbf{u}_k$$

$$\overline{\mathbf{x}}_{k+1} = \mathbf{\Phi}\hat{\mathbf{x}}_k + \mathbf{u}_k$$

We used:

$$\mathbf{h}^r\left(\hat{\mathbf{x}}_{k-1}, \overline{\mathbf{x}}_k\right) = \left[\mathbf{H}_{GPS}^r\hat{\mathbf{x}}_{k-1} + \mathbf{H}_{GPS}\mathbf{u}_k \quad \mathbf{h}_{LAS}(\overline{\mathbf{x}}_k)\right]^T,$$

where $\mathbf{H}_{GPS}^r$ and $\mathbf{H}_{GPS}$ are the rows of the pseudo-observation and observation matrices corresponding to the GPS measurements (derived using (9) and (15)).

The resulting cross-track positioning error ($x_V - \hat{x}_V$) is plotted Fig. 11.c). Note that the covariance envelopes are specific to the results of the data association.

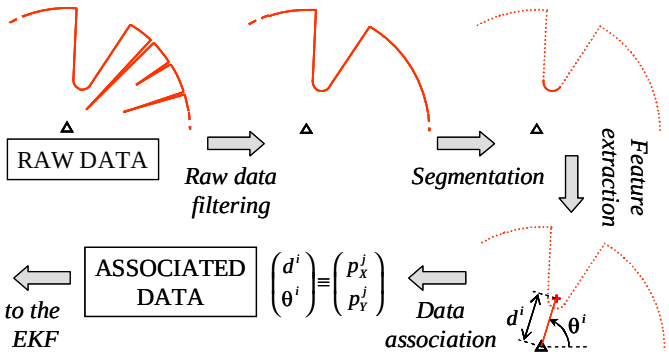

Fig. 10. Raw measurement processing and data association.

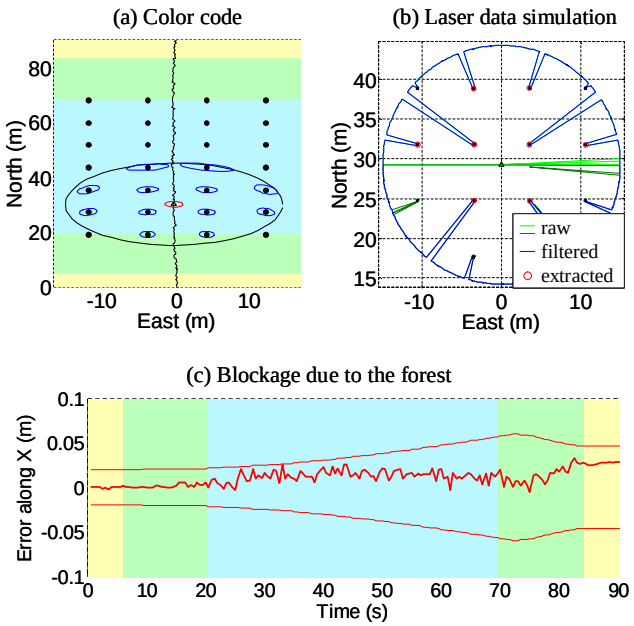

Fig. 11. Direct simulation example.

Monte-Carlo simulations results are determined using the standard deviation of the cross-track error at the exit of the laser-only (blue) area over 100 trials. These results are listed Table II and plotted Fig. 6 for comparison with the covariance analysis. Though the performance values are worse, the trends highlighted in Table II are all confirmed. In Fig. 6, the covariance and Monte-Carlo results start diverging for forest-length larger than 100 meters. This is to be expected because failures in data association, which is based on the predicted vehicle position estimate (see (16) in Appendix II for details), are more likely to occur when the vehicle position error increases.

So finally, we achieved one of this paper's main objectives in determining that, for a wide range of configurations, the laser/GPS integration enables to maintain sub-meter accuracy over GPS-outages as long as several hundreds of meters.

VI. Experimental Testing

Testing is carried out at the Illinois Institute of Technology. The two laser-scanners and the GPS antenna are assembled as described in Appendix II and mounted on an existing AGV platform equipped with a dual-frequency GPS receiver (Fig. 12). An embedded computer onboard the vehicle records all the measurements including the raw GPS data from the reference station transmitted via wireless spread-spectrum data-link. Synchronization and measurement projections on a common reference sample time are achieved using the computer's clock.

Truth vehicle trajectory and landmark locations are obtained using a fixed CPDGPS solution (Fig. 13.a). Because there is actually no physical obstruction to the sky, satellite masking for the GPS/laser integration system is performed artificially using the same model as in the simulations (Fig. 4.b).

Tree trunks are reproduced using five cardboard columns and one garbage can. It is interesting to note from Fig. 13.b), that the dark plastic garbage can (identification number 6) spent significantly less time in view of the laser scanner in spite of its larger diameter. This is explained by the difference in materials and colors [19].

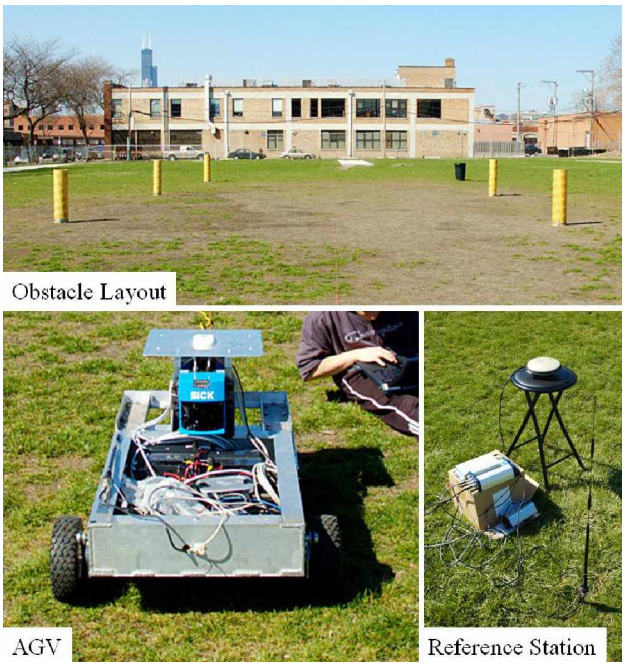

Fig. 12. Experimental setup.

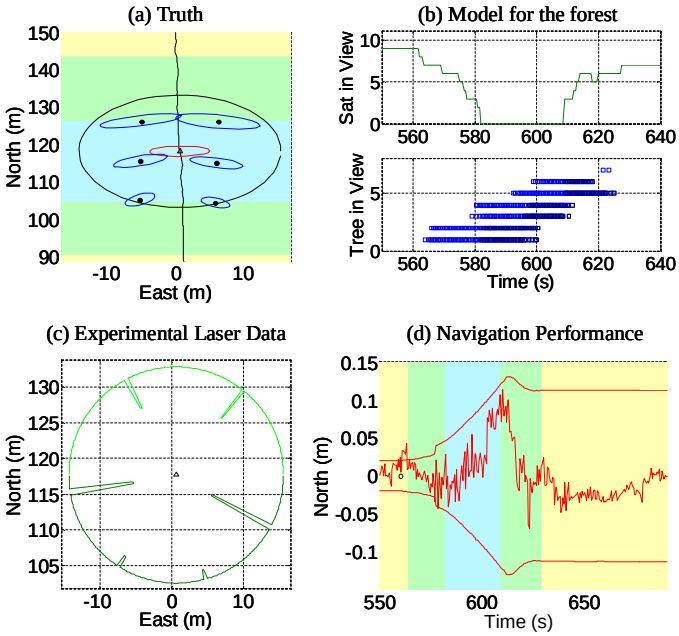

Fig. 13 Experimental data.

Fig. 13.d) confirms that smooth transitions between the open-sky and GPS-unavailable areas are achieved. The position error does not exceed 15 cm in spite of 30 meters of GPS outage.

Trials using the direct simulation with an identical setup are entirely consistent with these results. But most important, the data conclusively validates this novel navigation algorithm and the range-domain integration of GPS and laser-scanner measurements.

VI. Conclusion

Laser-augmented CPDGPS increases greatly the availability of sub-meter navigation solutions in outdoor environments. In partially obstructed GPS areas, the proposed range-domain integration exploits satellite signals that are not used in other implementations, by utilizing additional laser measurements. This improvement in positioning performance has been consistently quantified using covariance analysis, Monte-Carlo simulations and experimental testing. Overall, the system achieves considerable increases in continuity, availability and accuracy of the final navigation solution.

Future work includes the implementation of more robust raw measurement processing and data association procedures in unstructured environments.

Aknowledgment

We thank Fang-Cheng Chan and Bart Kempny for their help with the testing. We are especially grateful to Samer Khanafseh for his priceless contributions to the acquisition of experimental data.

Appendix I

The linearized laser measurement equation is

$$\begin{bmatrix}\boldsymbol{\delta d}\\ \boldsymbol{\delta\theta}\end{bmatrix}=\begin{bmatrix}\mathbf{F_d}(\mathbf{j}) & \mathbf{0} & \mathbf{F_d}(\mathbf{l})\\ \mathbf{F_\theta}(\mathbf{j}) & \mathbf{1}^{\mathbf{n_L}} & \mathbf{F_\theta}(\mathbf{l})\end{bmatrix}\begin{bmatrix}\boldsymbol{\delta x_{V,POS}}\\ \delta\phi_V\\ \boldsymbol{\delta p}\end{bmatrix}+\begin{bmatrix}\mathbf{v_d}\\ \mathbf{v_\theta}\end{bmatrix}$$

We use the following notation: consider a $n_L \times 2$ matrix $\mathbf{F_A}$ whose elements are A_X^i and A_Y^i. We have:

$$\mathbf{F_A}(\mathbf{j})=\begin{bmatrix}A_X^1 & \mathbf{i} & A_X^{n_L}\\ A_Y^1 & \mathbf{i} & A_Y^{n_L}\end{bmatrix}^{\mathbf{T}}$$

and $\mathbf{F_A}(\mathbf{l})=\begin{bmatrix}A_X^1 & A_Y^1 & \mathbf{0} & \mathbf{0} & \mathbf{0} & \mathbf{0}\\ \mathbf{0} & \mathbf{0} & \mathbf{l} & \mathbf{l} & \mathbf{0} & \mathbf{0}\\ \mathbf{0} & \mathbf{0} & \mathbf{0} & \mathbf{0} & A_X^{n_L} & A_Y^{n_L}\end{bmatrix}$. The elements of $\mathbf{F_d}$ are $\frac{\overline{p_X^i}-\bar{x}_V}{\left|\overline{\mathbf{p^i}}-\bar{\mathbf{x}}_{\mathbf{V,POS}}\right|}$ and $\frac{\overline{p_Y^i}-\bar{y}_V}{\left|\overline{\mathbf{p^i}}-\bar{\mathbf{x}}_{\mathbf{V,POS}}\right|}$ and the elements of $\mathbf{F_\theta}$ are $\frac{\overline{p_Y^i}-\bar{y}_V}{\left|\overline{\mathbf{p^i}}-\bar{\mathbf{x}}_{\mathbf{V,POS}}\right|^2}$ and $-\frac{\overline{p_X^i}-\bar{x}_V}{\left|\overline{\mathbf{p^i}}-\bar{\mathbf{x}}_{\mathbf{V,POS}}\right|^2}$.

where $\bar{x}$ is the predicted value of x and

$$\mathbf{p^i}=\begin{bmatrix}p_X^i & p_Y^i\end{bmatrix}^{\mathbf{T}} \quad \text{and} \quad \mathbf{x_{V,POS}}=\begin{bmatrix}x_V & y_V\end{bmatrix}^{\mathbf{T}}.$$

Appendix II

A. Raw laser measurement processing

A laser-scanner emits pulsed infrared laser beams that are reflected from surfaces of nearby objects and returned to the scanner. Signal time-to-return measurements are used to determine distances to the reflecting objects. The precision of the ranging measurement is affected by target surface properties (color, material reflectivity) and by the angle of incidence of the laser on the target surface. The pulsed laser beam is deflected with a rotating mirror to enable two-dimensional scanning [18].

In order to obtain a full 360° laser san, we assemble two 180° laser-scanners back-to-back. The GPS antenna is mounted in the alignment of the front laser's axis. The lever-arm distance between the two lasers is included in the model. We use the mm-mode configuration described in Table I.

Raw experimental data, especially in indoor environments contain some clutter (impulse noise). A careful laser calibration and a straightforward noise rejection filter eliminate this problem. The latter filter also gets rid of the mixed-pixel interferences, which occurs when a single beam is spanning on two surfaces at different depths.

Based on a predefined threshold between consecutive measurements, the data is then segmented. Each segment of the laser scan that is closer than the range limit designates a potential obstacle. The minimum number of measurements per segment n_{MIN} is defined by the rounded value of:

$$\sin^{-1}\left(\frac{2r_{MIN}}{\theta_{RES}\left(d_{MAX}-r_{MIN}\right)}\right)$$

where θ_{RES} is the angular resolution in radians, r_{MIN} is the predefined minimum obstacle radius, and d_{MAX} is the laser range limit. We consider that segments made of more than n_{MIN} measurements correspond to actual landmarks.

The segment's measurements can then be used to extract various landmark features. In our case, landmarks are vertical

cylinders. Therefore, the measurement of the distance to the cylinder's axis in a horizontal plane is the sum of the segment's minimum range value and the estimated obstacle radius (here the obstacle radius is known). This measurement is fed into the estimator according to the data association process.

B. Data Association

Data association is a challenging process, which if unsuccessful, leads to catastrophic navigation errors. The fact that we operate in a structured environment alleviates some of the difficulties and a simple yet efficient nearest neighbor approach [20] is sufficient to obtain satisfactory results.

For each measurement j and for each previously estimated landmark i, we compute the Mahalanobis distance (or normalized innovation square):

$$\rho^{i,j} = \left(\boldsymbol{\nu}^{i,j}\right)^{T} \cdot \left(\bar{\mathbf{Z}}^{i}\right)^{-1} \cdot \boldsymbol{\nu}^{i,j}$$

where $\boldsymbol{\nu}^{i,j} = \mathbf{z}^{j} - \bar{\mathbf{z}}^{i}$.

$\bar{\mathbf{z}}^{i} = \mathbf{h}_{LAS}(\bar{\mathbf{x}})$ is the best projected estimate of the laser measurement vector obtained from the non-linear equations (2) and (3).

The matrix $\bar{\mathbf{Z}}^{i}$ is made of the elements of $\bar{\mathbf{Z}}$ corresponding to landmark i, with:

$$\bar{\mathbf{Z}} = \mathbf{H}\bar{\mathbf{P}}\mathbf{H}^{T} + \mathbf{V}$$

We associate measurement j with landmark i if $\rho^{i,j}$ is a minimum for all measurements. In the case where there are more landmarks than measurements, a routine ensures that one measurement is not associated with more than one landmark. Besides, the Mahalanobis distance $\rho^{i,j}$ follows a chi-square probability distribution, with two degrees of freedom in our case. Therefore, the association is validated only if $\rho^{i,j}$ is lower than a predefined threshold corresponding to a desired confidence level.

If a measurement is associated but not validated, it is not used. If it is not associated, it is interpreted as a new landmark, and given a new identification number.

REFERENCES

[1] M. O'Connor, "Carrier-Phase Differential GPS for Automatic Control of Land Vehicles," *PhD Dissertation*, Stanford University, 1997

[2] T. Bell, "Precision Robotic Control of Agricultural Vehicles on Realistic Farm Trajectories," *PhD Dissertation*, Stanford University, 1999.

[3] G. R. Opshaug, and P. Enge, "Robotic Snow Cat," *Proc. ION GPS 2000*, Salt Lake City, UT, 2000.

[4] J. A. Farrell, T. Han-Shue, and Y. Yunchun, "Carrier Phase GPS-Aided INS-Based Vehicle Lateral Control," *Journal of Dynamic Systems, Measurement, and Control*, Transactions of the ASME, Vol. 125, pp. 339-353, 2003.

[5] R. Hirokawa, K. Nakakuki, K. Sato, and R. Ishihara, "Threading the Maze, GPS/INS, Landmark Sensing, and Obstacle Avoidance" *GPS World*, Vol. 15, No. 11, pp. 20-26, November 2004.

[6] Greenspan, R., "GPS and Inertial Integration," *The Global Positioning System: Theory and Applications*, B. W. Parkinson, J. J. Spilker, Jr., P. Axelrad, P. Enge, editors, AIAA Progress in Aeronautics and Astronautics Volume 163-4, Washington, DC, 1996

[7] I. Tena Ruiz, Y. Petillot, D. M. Lane, and C. Salson, "Feature Extraction and Data Association for AUV Concurrent Mapping and Localisation," *Proc. IEEE-ICRA*, 2001

[8] S. Thrun, "Robotic Mapping: A Survey," *Exploring Artificial Intelligence in the New Millenium*, G. Lakemeyer and B. Nebel, February 2002.

[9] R. Madhavan, H. Durrant-Whyte, and G. Dissanayake, "Natural Landmark-based Autonomous Navigation using Curvature Scale Space," *Proc. IEEE-ICRA*, 2002.

[10] S. B. Williams, G. Dissanayake, H. Durrant-Whyte, "An efficient Approach to the Simultaneous Localisation and Mapping Problem," *Proc. IEEE-ICRA*, 2002.

[11] M. Joerger, J. Christ, R. Duncan, and B. Pervan, "Integrated Design of an AGV for Improved GPS-based Path-Following Performance," *International Journal of Vehicle Design*, in press.

[12] M. Joerger, J. Christ, R. Duncan, and B. Pervan, "Design of an AGV for Improved CDGPS-based Control Performance," *Proc. ION GNSS*, September 2004.

[13] D. Lawrence, "Aircraft Landing Using GPS: Development and Evaluation of a Real Time System for Kinematic Position using the Global Positioning System", *PhD Dissertation*, Stanford University, 1996

[14] A. E. Bryson and L. J. Henrikson, "Estimation Using Sampled Data Containing Sequentially Correlated Noise," *AIAA J. Spacecraft*, Vol. 5. No. 6, June 1968.

[15] A. E. Bryson, *Applied Linear Optimal Control*, Cambridge University Press, 2002.

[16] A. Gelb, (editor), "Optimal Linear Filtering", *Applied Optimal Estimation*, The MIT Press, 1974.

[17] B. Pervan, and B. Parkinson, "Cycle Ambiguity Estimation for Aircraft Precision Landing Using the Global Positioning System," *AIAA J. of Guidance, Controls, and Dynamics*, Vol. 20, No. 4, pp 681-689, 1997.

[18] K. Bossert, "Reclaiming Kaho'olawe", *Geospatial Solutions*, Vol. 14, No. 9, September 2004.

[19] C. Ye, and J. Borenstein, "Characterization of a 2-D Laser Scanner for Mobile Robot Obstacle Negotiation," *Proc. IEEE-ICRA*, May 2002.

[20] Y, Bar-Shalom, and T. E. Fortmann, "Tracking and Data Association," *Mathematics in Science and Engineering*, Vol. 179, Academic Press, 1988.